# Further Comparison of Two Synoptic Surface Wind and Pressure Analysis Methods

JENNIFER M. CRAM AND ROGER A. PIELKE

*Department of Atmospheric Science, Colorado State University, Fort Collins, Colorado*

19 April and 11 October 1988

ABSTRACT

The geostrophic stream and potential functions of Sangster and the derived flat pressure field of Pielke and Cram are further compared. A simple numerical experiment with an idealized mountain–atmosphere system compares the two methods and their sensitivity to lateral boundary conditions. The flat pressure field of Pielke and Cram is essentially equivalent to the streamfunction of Sangster, although the two methods have different boundary condition formulations and resulting different sensitivities to these boundary conditions.

## 1. Introduction

Mean sea level (MSL) pressure analyses are regularly used despite the problems of reduction in areas of elevated terrain. The standard reduction method involves an assumed lapse rate from the ground surface to MSL and can lead to a large difference between the true horizontal pressure gradient at the surface and that inferred from the gradient of MSL-reduced pressure. Statistical adjustments such as the National Weather Service's plateau correction (Manual and Barometry 1963) or different lapse rate estimates may reduce, but do not completely eliminate, this difference. Two related surface analysis methods that attempt to circumvent the problem with a different approach are those of Sangster (1960, 1987; hereafter referred to as SAN) and Pielke and Cram (1987, hereafter referred to as PC). The SAN method essentially decomposes the surface geostrophic wind field into streamfunction and potential fields (the geostrophic wind on a nonflat terrain surface has both nondivergent and irrotational components) while the PC method calculates a streamfunction-like pressure field. Davies-Jones (1988) has shown theoretically that PC's pressure field and SAN's streamfunction are essentially equivalent. Lynch (1988) also reviews Sangster's method and the general problem of partitioning a wind field into streamfunction and potential fields.

The purpose of this paper is to compare the PC and SAN methods numerically with an idealized mountain–atmosphere system, and to test their sensitivity to lateral boundary conditions.

## 2. Analytical comparison of SAN and PC methods

The similarities and differences between the SAN and PC methods will be briefly reviewed in this section.

*Corresponding author address:* Dr. Jennifer M. Cram, Dept. of Atmospheric Science, Colorado State University, Fort Collins, CO 80523.

Both methods are based upon a decomposition of the surface geostrophic wind. From PC, the surface geostrophic wind (along $\sigma = 1$) is represented by

$$u_g = -\frac{\theta}{f}\frac{\partial \pi}{\partial y}\bigg|_\sigma - \frac{g}{f}\frac{\partial z_G}{\partial y}$$

$$v_g = \frac{\theta}{f}\frac{\partial \pi}{\partial x}\bigg|_\sigma + \frac{g}{f}\frac{\partial z_G}{\partial x}, \tag{1}$$

where $u_g$ and $v_g$ are the winds in the west–east ($x$) and south–north ($y$) directions, $f$ is the Coriolis parameter, $\theta$ is potential temperature, $\pi = c_p T/\theta = c_p(p/p_0)^\gamma$, $\gamma = R/c_p$, $g$ is the gravitational constant, and $z_G$ is surface elevation. Pielke and Cram use these calculated winds to solve a Poisson equation for the pressure field $\tilde{\pi}$:

$$\nabla_\sigma^2 \tilde{\pi} = \frac{\partial}{\partial x}\left(\frac{fv_g}{\theta}\right)\bigg|_\sigma - \frac{\partial}{\partial y}\left(\frac{fu_g}{\theta}\right)\bigg|_\sigma. \tag{2}$$

Equation (2) is used in the actual calculations for $\tilde{\pi}$, but for comparison purposes substituting (1) into (2), and ignoring the variation of $f$ with latitude, results in

$$\nabla_\sigma^2 \tilde{\pi} = \nabla_\sigma^2 \pi + \frac{g}{\theta}\nabla^2 z_G - \frac{g}{\theta^2}\left(\frac{\partial z_G}{\partial x}\bigg|_\sigma \frac{\partial \theta}{\partial x}\bigg|_\sigma + \frac{\partial z_G}{\partial y}\bigg|_\sigma \frac{\partial \theta}{\partial y}\bigg|_\sigma\right). \tag{3}$$

The SAN method can be looked at similarly. Defining a streamfunction $\psi$ along a $\sigma$ surface (equivalent to a scaled Sangster, 1960 H field), then

$$\nabla_\sigma^2 \psi = \frac{\partial v_g}{\partial x}\bigg|_\sigma - \frac{\partial u_g}{\partial y}\bigg|_\sigma. \tag{4}$$

Likewise, the potential $\chi$ (equivalent to a scaled Sangster, 1960 G field) may be defined by

$$\nabla_\sigma^2 \chi = \frac{\partial u_g}{\partial x}\bigg|_\sigma + \frac{\partial v_g}{\partial y}\bigg|_\sigma. \tag{5}$$

Substituting (1) into these equations (again ignoring the variation of $f$ with latitude) results in

$$\nabla_\sigma^2\psi = \frac{\theta}{f}\nabla_\sigma^2\pi + \frac{g}{f}\nabla^2 z_G + \frac{1}{f}\left(\frac{\partial\pi}{\partial x}\bigg|_\sigma \frac{\partial\theta}{\partial x}\bigg|_\sigma + \frac{\partial\pi}{\partial y}\bigg|_\sigma \frac{\partial\theta}{\partial y}\bigg|_\sigma\right) \quad (6)$$

$$\nabla_\sigma^2\chi = \frac{1}{f}\left(\frac{\partial\pi}{\partial x}\bigg|_\sigma \frac{\partial\theta}{\partial y}\bigg|_\sigma - \frac{\partial\pi}{\partial y}\bigg|_\sigma \frac{\partial\theta}{\partial x}\bigg|_\sigma\right) = \frac{1}{f}J_\sigma(\pi,\theta). \quad (7)$$

Thus, although (6) and (3) are similar, they are not exactly equivalent unless $\partial\theta/\partial x = \partial\theta/\partial y = 0$, in which case the divergent component of the wind is zero. As both Doswell (1988) and Davies-Jones (1988) have pointed out, the geostrophic divergence on a sigma surface is due to baroclinicity and the $p-\alpha$ (or in this case $\pi-\theta$) solenoids. The PC method is closely (but not exactly) retrieving a scaled streamfunction [(3) is not exactly the same as $f/\theta*(6)$], and thus cannot represent the irrotational component of the surface geostrophic wind. Davies-Jones (1988) shows that the PC method retrieves a scaled streamfunction for surface geostrophic mass flux while the SAN method retrieves a scaled streamfunction for surface geostrophic wind.

In the next section another aspect of the PC method will be discussed, and in section 4 the PC and SAN methods will be compared numerically.

### 3. Further note on PC method

The $\tilde{\pi}$ field derived by PC is interpreted as a "flat ground surface pressure field"; yet as it is derived in PC and in (2) it is a $\sigma$ surface field. A plausible alternative (plausible a priori; it turns out to be trivial) would be to define the $\tilde{\pi}$ field (with appropriate boundary conditions) as

$$\nabla_z^2\tilde{\pi} = \frac{\partial}{\partial x}\left(\frac{fv_g}{\theta}\right)\bigg|_z - \frac{\partial}{\partial y}\left(\frac{fu_g}{\theta}\right)\bigg|_z \quad (8)$$

where $\theta$, $u_g$, and $v_g$ must be interpolated to the fixed height at each $\tilde{\pi}$ point. As the right-hand side of this equation is known only on $\sigma$ surfaces, the interpolation is performed using the chain rule, i.e.,

$$\nabla_z^2\tilde{\pi} = \frac{\partial}{\partial x}\left(\frac{fv_g}{\theta}\right)\bigg|_\sigma - \frac{\partial}{\partial y}\left(\frac{fu_g}{\theta}\right)\bigg|_\sigma - \frac{\partial}{\partial z}\left(\frac{fv_g}{\theta}\right)\frac{\partial z_G}{\partial x} + \frac{\partial}{\partial z}\left(\frac{fu_g}{\theta}\right)\frac{\partial z_G}{\partial y}. \quad (9)$$

Since $u_g$ and $v_g$ are defined in $z$ coordinates as

$$u_g = -\frac{\theta}{f}\frac{\partial\pi}{\partial y}\bigg|_z, \qquad v_g = \frac{\theta}{f}\frac{\partial\pi}{\partial x}\bigg|_z, \quad (10)$$

then by substitution into (8)

$$\nabla_z^2\tilde{\pi} = \nabla_z^2\pi. \quad (11)$$

At first glance this would seem to be a more clear-cut field to retrieve [than the $\tilde{\pi}$ defined by (3)]; the horizontal Laplacian of $\pi$ at each point on the $z$ surface. However, the simple experiment described below shows the problem with that definition.

A three-dimensional atmosphere was specified on an Arakawa "C" grid. The horizontal grid mesh was 71 by 71 points (3.333 km grid interval) with 13 vertical levels on $z$ surfaces from 0 to 6000 m. A standard atmosphere base state ($\partial T/\partial z = -6.5°\text{C km}^{-1}$) was superimposed on a specified constant MSL pressure gradient and a constant horizontal $\theta$ gradient throughout the atmosphere. These parameters were varied for each experiment and are listed in Table 1. An idealized mountain (shown in Fig. 1) was superimposed on the atmosphere and the $\pi$ and $\theta$ fields were interpolated to the mountain surface. The surface [and also the $\sigma = 0.9$ level for the above PC-modified method because of the need for a vertical difference in (9)] geostrophic winds were calculated using (1), and Eqs. (2), (9), and (6) and (7) were used to derive the PC, PC-modified (PC-M), and SAN fields, respectively. The derived fields should not, and will not, look like the base state MSL pressure field. That field is only used to create the three-dimensional atmosphere. The imposed horizontal $\theta$ gradient results in a changing horizontal pressure gradient with height, and thus a changing horizontal pressure gradient along the mountain surface. The (a priori) aim of the PC, PC-M, and SAN fields is to represent this horizontal pressure gradient information in the surface pressure field. The surface wind, $\pi$, and $\theta$ fields on the mountain surface are not representative of the "real" fields that would exist in the presence of a physical mountain, but the purpose of this paper is simply to compare the different methods.

The lateral boundary condition for the PC method's $\tilde{\pi}$ field is simply the known (in this case, reduced otherwise) zero-elevation $\pi$ (pressure) at the boundaries. Neumann boundary conditions are used for the $\psi$ field of the SAN method using the calculated geostrophic winds. The potential field ($\chi$) boundary conditions are derived using the difference between the total geostrophic wind $\mathbf{V}_g$ and the $\mathbf{V}_\psi$ calculated from the derived $\psi$ field (as suggested by Sangster 1960). This effectively works out that $\chi_B = 0$; the small deviation of $\chi_B$ from zero is a result of numerical discretization and numerical $\psi$ solution errors. The $\pi$, $\psi$, and $\chi$ fields are all solved by sequential relaxation.

The "atmosphere" for this first experiment was set so that $\partial p_{\text{MSL}}/\partial y = 0.005$ mb km$^{-1}$ and $\partial\theta/\partial y = 0.0025°\text{C km}^{-1}$. This results in an increasing pressure gradient with height, but a constant north–south gradient at each height level. The MSL, or base state, pressure gradient is shown in Fig. 3a. The deviation of the surface geostrophic winds from $\mathbf{V}_{\text{MSL}}$, $(\mathbf{V}_g - \mathbf{V}_{\text{MSL}})$,

TABLE 1. Description of experiment parameters.

| Expt | $\frac{\partial p_{MSL}}{\partial y}$ (0.001 mb km$^{-1}$) | $\theta$ gradient (0.001°C km$^{-1}$) | $\frac{\partial T}{\partial z}$ (°C km$^{-1}$) | Mountain location | Purpose |
|---|---|---|---|---|---|
| 1 | 5.0 | $\frac{\partial \theta}{\partial y} = 2.5$ | −6.5 | Middle | Compare PC, PC-M, SAN |
| 2 | 5.0 | $\frac{\partial \theta}{\partial x} = 2.5$ | −6.5 | Middle | Compare PC, SAN |
| 3 | 5.0 | $\frac{\partial \theta}{\partial x} = 2.5$ | −6.5 | Side | Sangster b.c. for SAN, $\chi_B = 0$ |
| 4 | 5.0 | $\frac{\partial \theta}{\partial x} = 2.5$ | −6.5 | Side | San.-opposite b.c. for SAN, $\psi_B = 0$ |
| 5 | 5.0 | $\frac{\partial \theta}{\partial x} = 2.5$ | −6.5 | Side | Neumann b.c. for SAN |
| 6 | 5.0 | $\frac{\partial \theta}{\partial y} = 2.5$ | −6.5 | Side | Dirichlet b.c. for PC |
| 7 | 5.0 | $\frac{\partial \theta}{\partial y} = 2.5$ | −8.0 | Side | Bad guess for PC b.c. |

reflects the increasing pressure gradient with height and is shown in Fig. 3b and in the cross section in Fig. 2a. The $V_{MSL}$ is simply due to the base state MSL pressure gradient and is 39.6 m s$^{-1}$ from east to west. The PC derived pressure field is shown in Fig. 3c. Although the PC method derives a $\pi$ field, all plots will be shown in terms of pressure, $p$. The PC-M derived pressure field is exactly the same as in Fig. 3a. The deviations of the PC and PC-M derived winds from the $V_{MSL}$ field are shown in Figs. 3d and 3e. $V_{PC\text{-}M}$ is the same as $V_{MSL}$, so the field shown in Fig. 3e is exactly zero. The SAN $\psi$ and $\chi$ fields are shown in Figs. 3f and 3h and their resulting wind component deviations from $V_{MSL}$ in Figs. 3g and 3i. The PC field is obviously very similar to the SAN $\psi$ field, and their respective winds differ by a maximum of less than 0.5 m s$^{-1}$. Although the PC-M pressure field is exactly the same as the base state MSL pressure field, it does not represent the increasing horizontal pressure gradient with height and, thus, the horizontal pressure gradient along the higher terrain. The PC pressure and SAN $\psi$ fields better represent the surface horizontal pressure gradient than the PC-M pressure field. The SAN $\chi$ field shows that there is an additional, non-negligible, irrotational surface wind component. The irrotational winds are actually on the same order as $V_\psi - V_{MSL}$ (Fig. 3g vs. Fig. 3i). By its

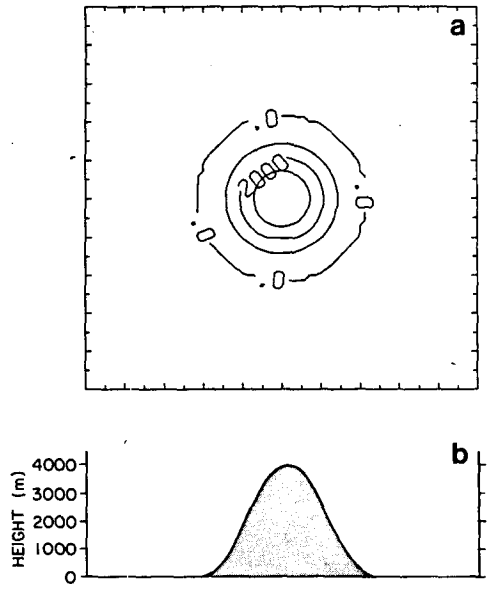


FIG. 1. (a) Surface elevation (m) for Experiments 1 and 2. Center point of mountain is at 4000 m; (b) cross section of mountain.

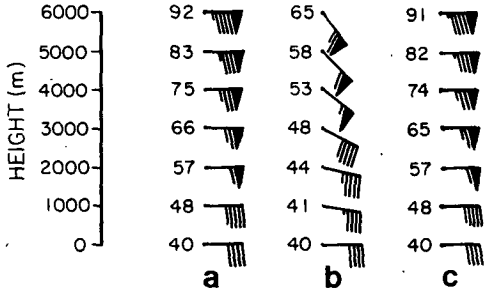


FIG. 2. Vertical geostrophic wind profiles for the seven experiments: (a) Experiments 1 and 6; (b) Experiments 2, 3, 4, 5; (c) Experiment 7. Wind barbs point in the direction the wind is blowing from (up is north). Long barbs are 10 m s$^{-1}$ and flags are 50 m s$^{-1}$.

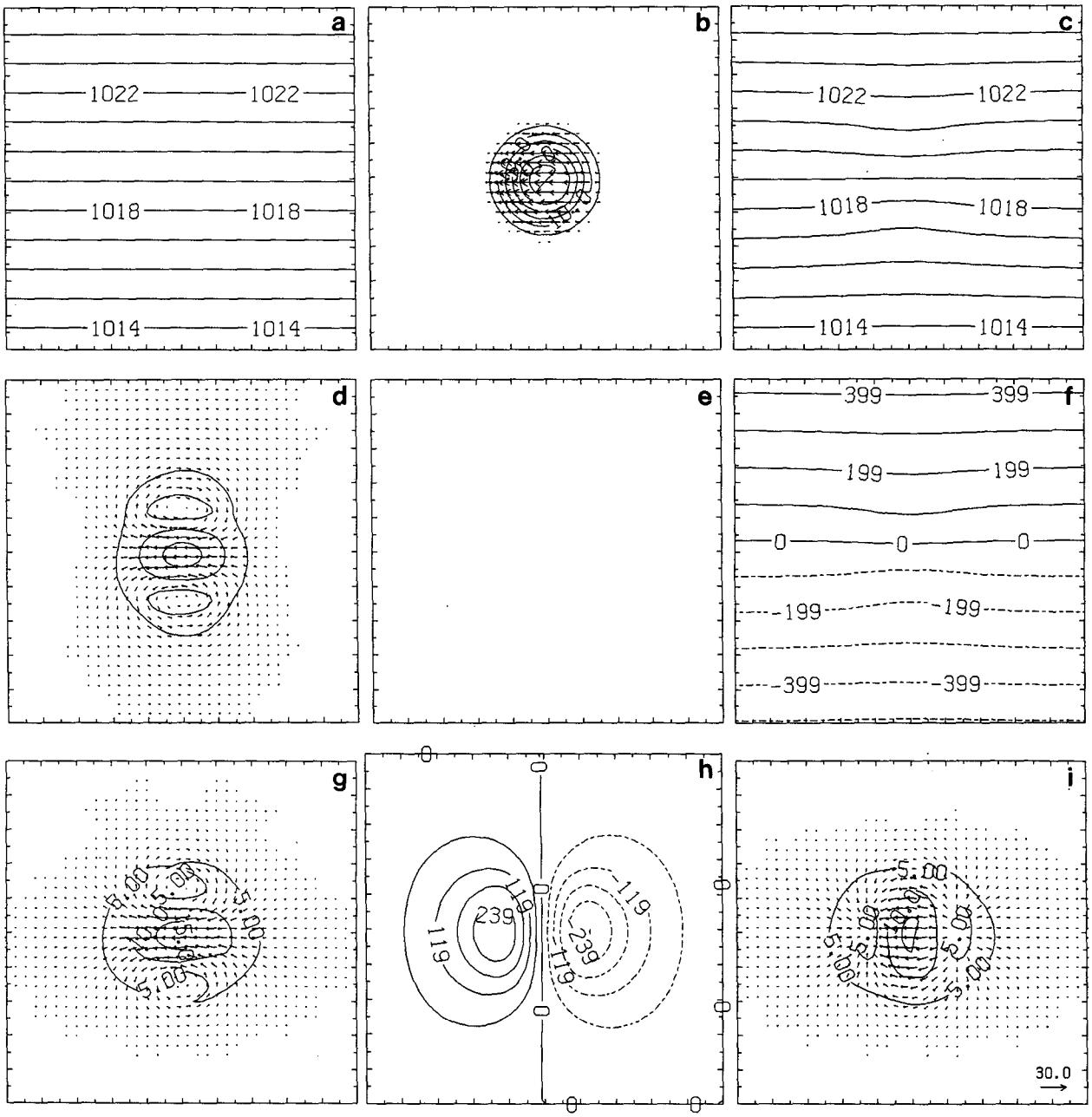


FIG. 3. Results from Experiment 1: (a) MSL pressure field (mb); (b) deviation of surface geostrophic wind from MSL geostrophic wind ($\mathbf{V}_g - \mathbf{V}_{MSL} = \mathbf{V}_g - 39.6$ m s$^{-1}$); (c) PC derived pressure field (mb); (d) deviation of PC derived geostrophic winds from $\mathbf{V}_{MSL}$: ($\mathbf{V}_{PC} - \mathbf{V}_{MSL}$); (e) deviation of PC-M derived geostrophic winds from $\mathbf{V}_{MSL}$: ($\mathbf{V}_{PC-M} - \mathbf{V}_{MSL}$); (f) streamfunction field $\psi$ ($10^4$ m$^2$ s$^{-1}$); (g) deviation of $\mathbf{V}_\psi$ from $\mathbf{V}_{MSL}$: ($\mathbf{V}_\psi - \mathbf{V}_{MSL}$); (h) potential field $\chi$ ($10^3$ m$^2$ s$^{-1}$); (i) $\mathbf{V}_\chi$. The wind vectors in each figure are scaled by the vector shown in the lower right corner of Fig. 3i, and all vector plots are contoured in isotach intervals of 5 m s$^{-1}$.

definition, the PC field cannot represent this. The PC-M field cannot retrieve the increasing-with-height pressure gradient information because it simply retrieves $\nabla_z^2\pi$, which vanishes at each vertical level even though the pressure gradient itself changes. Thus, the PC method, as compared to the PC-M method, better represents the surface horizontal pressure gradient and the surface geostrophic wind field.

## 4. Numerical experiments

An experiment was described in section 3 to compare the PC and PC-M methods. Several other experiments will be described here to compare the PC and SAN methods further, and to investigate their sensitivity to lateral boundary conditions. Unless otherwise noted, the numerical setup and parameters are the same as

described in section 3. The experiments are outlined in Table 1. Here $V_{MSL}$ is 39.6 m s$^{-1}$ from east to west in all the experiments.

The parameters in the second experiment are set so that $\partial p_{MSL}/\partial y = 0.005$ mb km$^{-1}$ and $\partial\theta/\partial x = 0.001$°C km$^{-1}$. This results in the pressure gradient changing orientation with height. The MSL pressure gradient is the same as in Fig. 3a; the surface wind deviation from $V_{MSL}$ (Figs. 4a and 2b) reflects the changing orientation with height. The PC pressure field and the SAN $\psi$ field are again very similar, just scaled differently (Figs. 4b and 4d). The deviation from $V_{MSL}$ of the winds derived from these fields is also very similar (Figs. 4c and 4e). The PC field again cannot reflect the information in the $\chi$ and $V_\chi$ fields (Figs. 4f and 4g). The goal in the PC method was to derive a pressure field consistent with conventional MSL pressure analyses. The geostrophic winds derived from such a pressure field are nondivergent except for the influence of the Coriolis effect.

An interesting difference between the PC $\tilde{\pi}$ field and the SAN $\psi$ field is the tilt of the isolines. The $\tilde{\pi}$ isolines curve only near the mountain while the $\psi$ isolines have a slight southeast–northwest tilt (Figs. 4b and 4d).

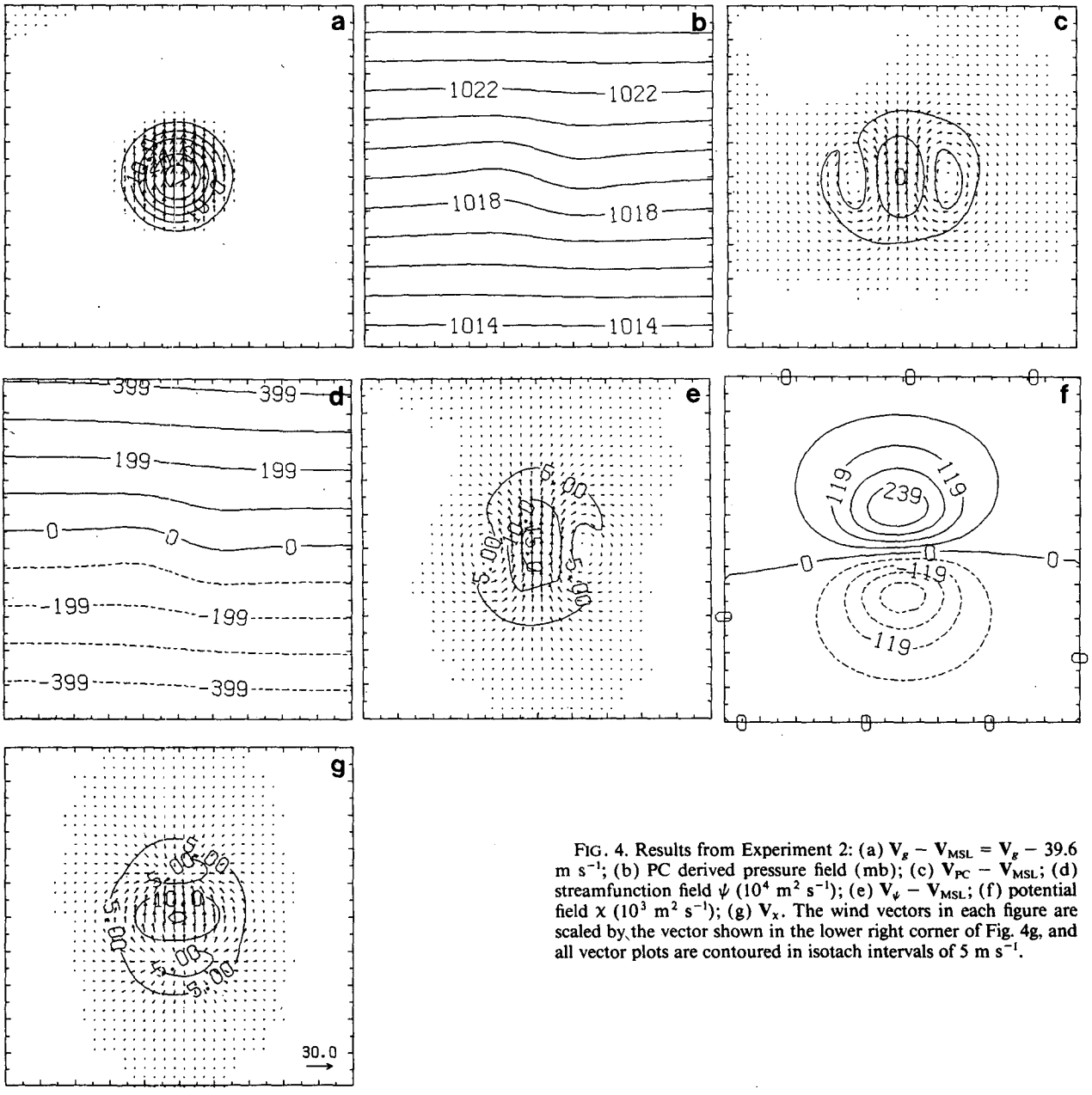


FIG. 4. Results from Experiment 2: (a) $V_g - V_{MSL} = V_g - 39.6$ m s$^{-1}$; (b) PC derived pressure field (mb); (c) $V_{PC} - V_{MSL}$; (d) streamfunction field $\psi$ ($10^4$ m$^2$ s$^{-1}$); (e) $V_\psi - V_{MSL}$; (f) potential field $\chi$ ($10^3$ m$^2$ s$^{-1}$); (g) $V_\chi$. The wind vectors in each figure are scaled by the vector shown in the lower right corner of Fig. 4g, and all vector plots are contoured in isotach intervals of 5 m s$^{-1}$.

These differences are due to the boundary conditions. The $\tilde{\pi}$ field is forced by a Dirichlet-type boundary condition while the $\psi$ field has a Neumann-type boundary condition. Boundary condition effects will be investigated more closely in the next few experiments.

### *a. Boundary condition experiments with the SAN method*

The division of the surface geostrophic wind into $\psi$ and $\chi$ fields by solution of the Poison equations requires lateral boundary conditions on the $\psi$ and $\chi$ fields. These boundary conditions determine the division of the surface geostrophic winds into their irrotational and nondivergent components along the $\sigma$ surface. The irrotational component is most significant over the steepest terrain. If there is no terrain near the boundary, the boundary winds can be assumed to be mostly nondivergent and one can use the tangential $\psi$ derivative information ($\partial\psi/\partial s = -\mathbf{V}_g \cdot \mathbf{n}$ where $s$ is the distance along the boundary and $\mathbf{n}$ is the normal unit vector) to integrate $\psi$ along the boundary. $\chi$ will be zero at the boundaries. Sangster (1960) suggested that a practical approach would be to let $\chi = 0$ along the boundaries, solve for $\chi$, calculate $\mathbf{V}_\chi$, then use the $\mathbf{V}_\psi$ information (from $\mathbf{V}_\psi = \mathbf{V}_g - \mathbf{V}_\chi$) to calculate $\psi$ around the boundaries for a Dirichlet-type boundary condition. Sangster points out that this method minimizes the contribution of the $\chi$ field to the solution. Although Sangster's suggested boundary condition may be appropriate when the near-boundary winds are easily seen to be mostly nondivergent, it may be inappropriate when there is a significant irrotational component. Sangster (1960) used the above described boundary conditions while Sangster (1987) used a MSL-reduced Dirichlet-type boundary condition.

The next two experiments illustrate the sensitivity of the $\psi$ and $\chi$ fields to these Dirichlet-type boundary conditions when a significant irrotational component crosses the boundary (e.g., induced by the mountain intersecting the boundary). Experiment 3 shows the effect of using Sangster's (1960) suggested boundary conditions and Experiment 4 is the opposite case (where it is initially assumed $\psi = 0$ on the boundaries). The mountain is shown in Fig. 5a. The other parameters are the same as in Experiment 2. The values of $\mathbf{V}_g - \mathbf{V}_{\text{MSL}}$ are shown in Figs. 5b and 2b.

The results from the two experiments are shown in Figs. 6 and 7 and are completely different. In both experiments, the Dirichlet boundary conditions for the "other" variable were integrated around the edges in opposite directions from the southwest to the northeast corners of the grid. The wind error in the northeast corner of Fig. 7d is due to the integrated $\chi$ boundary values (around the boundaries from the southwest corner) not matching exactly, and that corner error propagating inward owing to the relaxation procedure. This error is not due to numerical truncation or discreti-

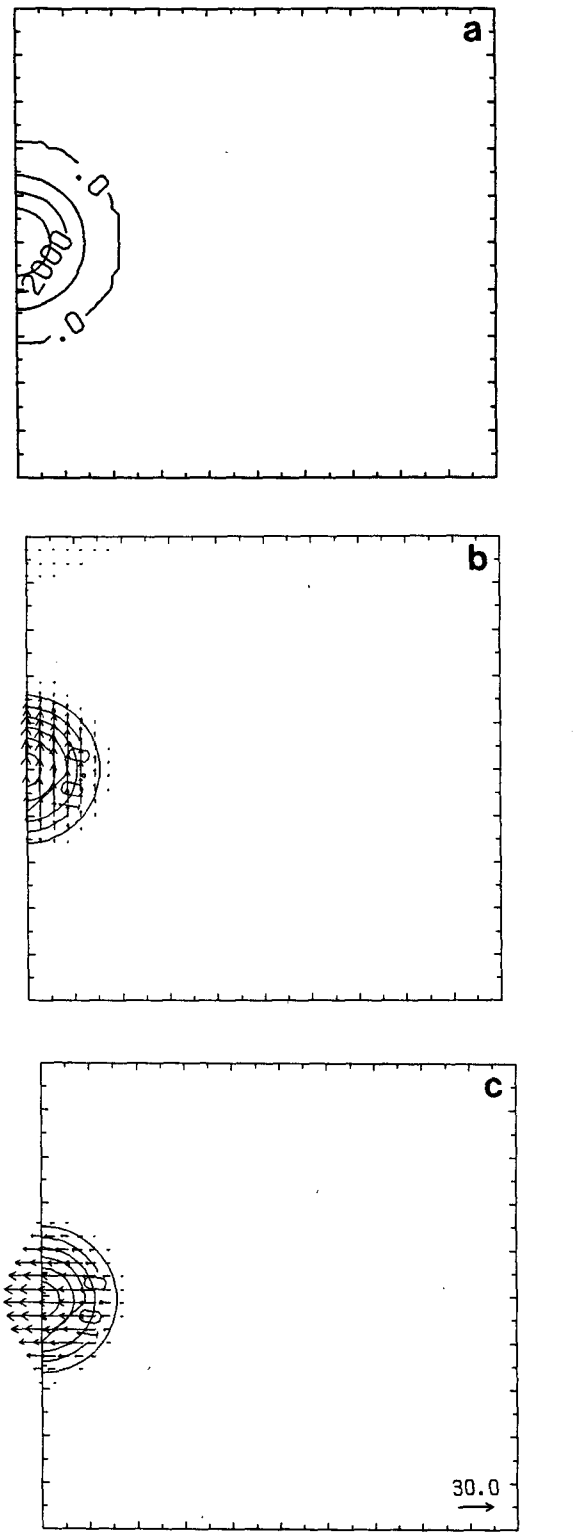


FIG. 5. (a) Surface elevation (m) for Experiments 3–7. Center point of the mountain is at 4000 m; (b) $\mathbf{V}_g - \mathbf{V}_{\text{MSL}}$ for Experiments 3–5; (c) $\mathbf{V}_g - \mathbf{V}_{\text{MSL}}$ for Experiments 6 and 7. The wind vectors in each figure are scaled by the vector shown in the lower right corner of Fig. 5c, and all vector plots are contoured in isotach intervals of 5 m s$^{-1}$.

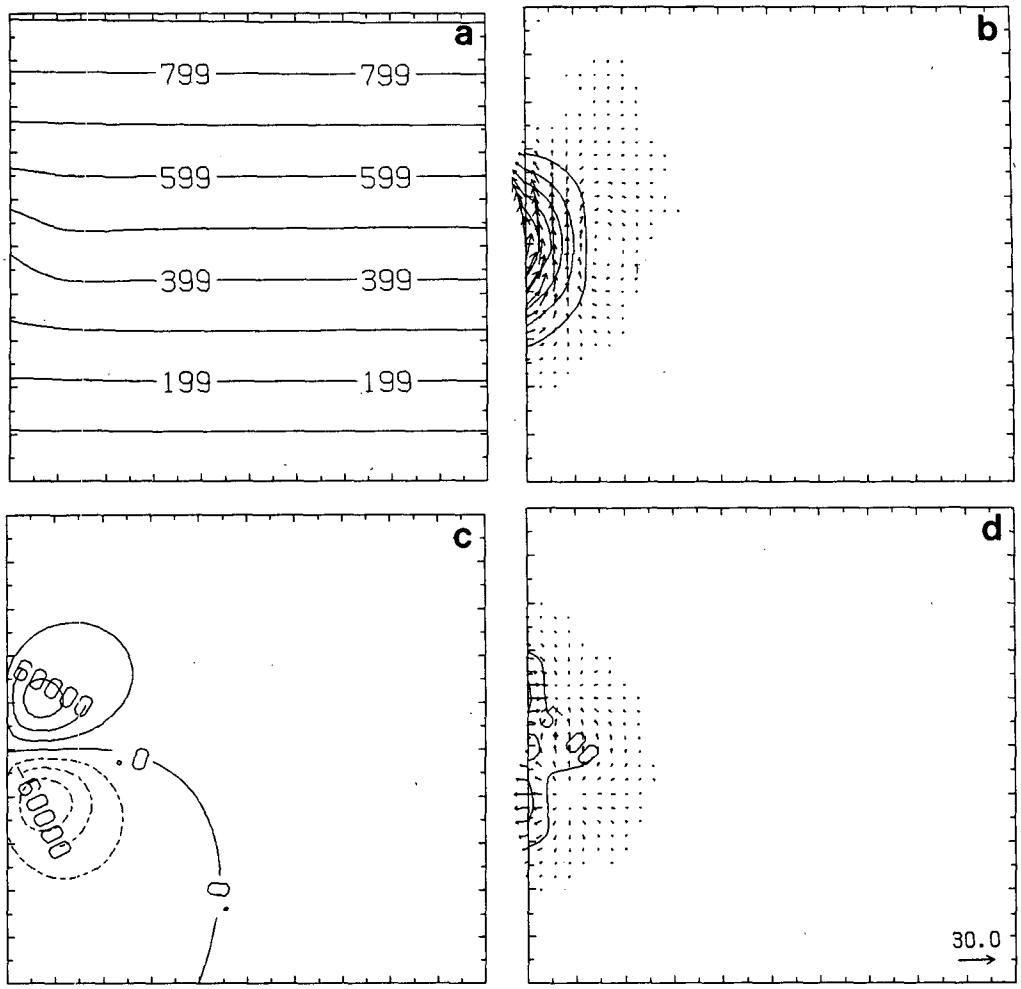


FIG. 6. Results from Experiment 3: (a) Streamfunction field $\psi$ ($10^4$ m$^2$ s$^{-1}$); (b) $\mathbf{V}_\psi - \mathbf{V}_{\mathrm{MSL}}$; (c) potential field $\chi$ (m$^2$ s$^{-1}$); (d) $\mathbf{V}_\chi$. The wind vectors in each figure are scaled by the vector shown in the lower right corner of Fig. 6d, and all vector plots are contoured in isotach intervals of 5 m s$^{-1}$.

zation; it occurs because an artificial (and incorrect) partition into $\mathbf{V}_\psi$ and $\mathbf{V}_\chi$ has been forced on $\mathbf{V}_g$ at the boundaries. As discussed by Lynch (1988), the input data (winds and calculated $\zeta = \mathbf{k}\cdot\nabla_\sigma \times \mathbf{V}_g$ and $\delta = \nabla_\sigma \cdot \mathbf{V}_g$) need to match an integral constraint in order for the boundary $\chi$ (or $\psi$) to be single-valued. In Experiment 4, the data need to match the constraint [(8) from Lynch]

$$\iint_\Omega \zeta da = \oint_{\partial\Omega} \mathbf{V}_s ds, \tag{12}$$

where $da$ is the area increment over the domain $\Omega$, $ds$ is the line increment along the domain boundary $\partial\Omega$, and $\mathbf{V}_s$ is the vector component parallel to the boundary. Likewise, the constraint for Experiment 3 is [(7) from Lynch]

$$\iint_\Omega \delta da = \oint_{\partial\Omega} \mathbf{V}_n ds, \tag{13}$$

where $\mathbf{V}_n$ is the vector component perpendicular to the boundary. As Lynch points out, an arbitrary $\zeta$, $\delta$, and $\mathbf{V}_B$ cannot be expected to satisfy the integral constraints (12) and (13) above, although $\mathbf{V}_B$, $\zeta_0$, and $\delta_0$ [where $\zeta_0$ and $\delta_0$ are derived from the solutions of (4) and (5) using $\mathbf{V}_B$] do satisfy the constraints. $\zeta$ and $\delta$ correspond to the original data. However, the original $\mathbf{V}_B$ has been modified (not the total $\mathbf{V}_B$, but its partitioning into $\mathbf{V}_\psi$ and $\mathbf{V}_\chi$, and thus $\mathbf{V}_n$ and $\mathbf{V}_s$) by imposing the boundary condition $\psi_B = 0$ (or $\chi_B = 0$). Thus $\mathbf{V}_B$ is no longer compatible with $\zeta$ and $\delta$, and the integrated $\chi_B$ (or $\psi_B$) is subsequently not single-valued.

The solution is to change the data ($\mathbf{V}_B$, $\psi_B$, or $\chi_B$, or the interior $\mathbf{V}_g$, $\zeta$, or $\delta$) to fulfill the constraint. Sangster (1960) distributed the integrated $\psi_B$ error (as in Experiment 3) evenly over all grid intervals. Davies-Jones (personal communication, 1988) has shown with variational analysis that the minimal data adjustment occurs with a uniform error distribution. However, the

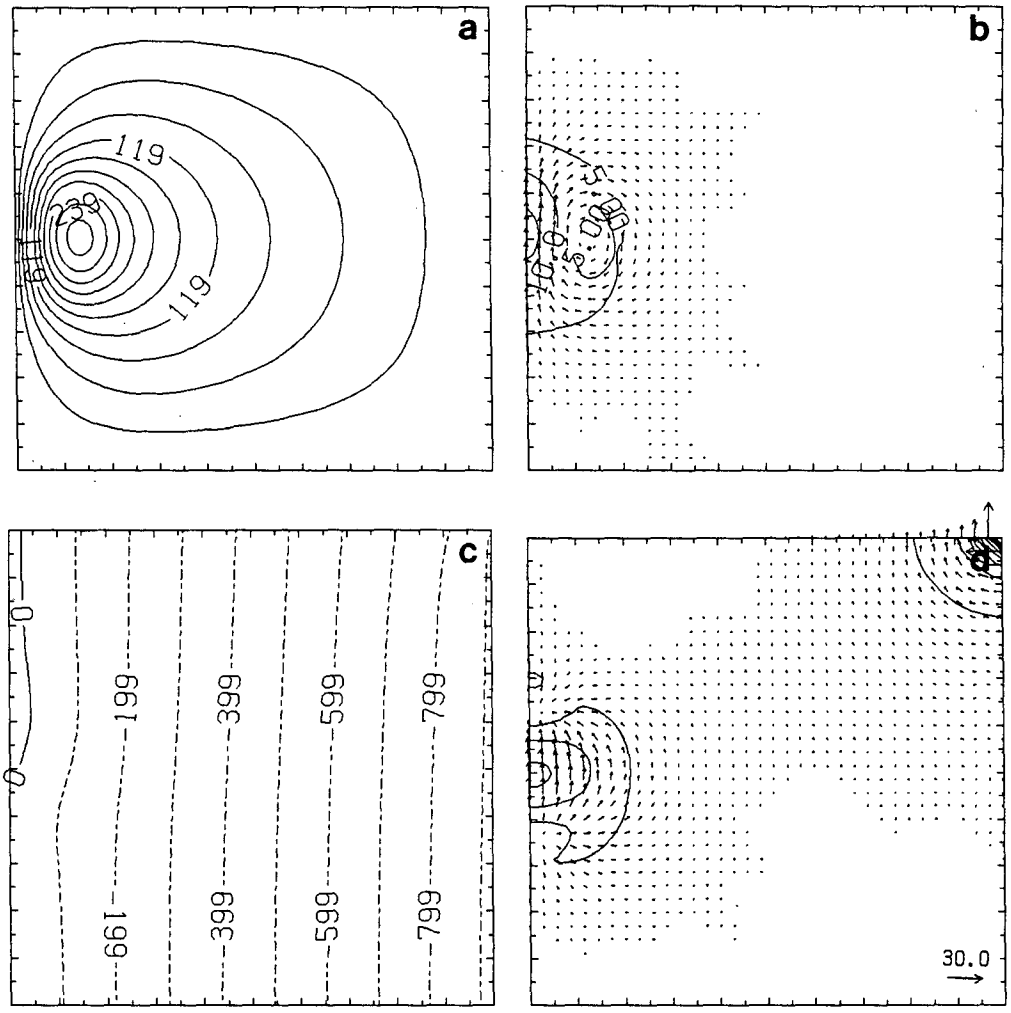


FIG. 7. Results from Experiment 4: (a) streamfunction field $\psi$ ($10^3$ m$^2$ s$^{-1}$); (b) $\mathbf{V}_\psi$; (c) potential field $\chi$ ($10^4$ m$^2$ s$^{-1}$); (d) $\mathbf{V}_\chi - \mathbf{V}_{MSL}$. Deviations above 50 m s$^{-1}$ are not plotted (upper right corner of Fig. 6d). The wind vectors in each figure are scaled by the vector shown in the lower right corner of Fig. 7d, and all vector plots are contoured in isotach intervals of 5 m s$^{-1}$.

$\chi_B$ error in Experiment 4 (and $\psi_B$ error in Experiment 3, although it is much smaller) occurs as a result of the incorrect partitioning of $\mathbf{V}_B$ into $\mathbf{V}_\psi$ and $\mathbf{V}_\chi$. This partitioning is not the same all the way around the boundary; the partitioning is most complex and least obvious along the mountain-boundary intersection. It is not apparent that an even error distribution would result in the most physically consistent $\psi$ and $\chi$ fields.

Aside from the boundary condition corner error, Experiments 3 and 4 result in very different divisions of $\mathbf{V}_g$ into $\mathbf{V}_\psi$ and $\mathbf{V}_\chi$, and very different $\psi$ and $\chi$ fields. This is due to the non-uniqueness of the solution. Lynch (1988) emphasizes that the streamfunction and potential fields can be modified arbitrarily, yet still together define the proper total wind.

Davies-Jones (1988) has suggested that the most appropriate boundary conditions for this problem are the Neumann conditions on the $\psi$ field ($\partial\psi/\partial n = \mathbf{V}_g \cdot \mathbf{s}$ where $n$ is the distance normal to the boundary and $\mathbf{s}$ is the tangential unit vector). In Experiment 5 the parameters and mountain are the same as in Experiments 3 and 4 above, but Neumann boundary conditions are used for the $\psi$ field. The $\chi$ boundary conditions are Dirichlet-type and determined from the difference between $\mathbf{V}_g$ and $\mathbf{V}_\psi$ (calculated from the derived $\psi$) where $\partial\chi/\partial s = (\mathbf{V}_g - \mathbf{V}_\psi) \cdot \mathbf{s}$. As stated previously, this effectively results in $\chi_B = 0$. Davies-Jones (1988) suggests setting $\chi_B = 0$ directly. The results are shown in Fig. 8 and are very similar to Fig. 6 (Experiment 3). Davies-Jones points out that these boundary conditions maximize the nondivergent component at the expense of the irrotational component whereas the opposite boundary conditions (Neumann boundary conditions on $\chi$ and $\psi_B = 0$) would maximize the irrotational component.

Ideally, the calculated $\psi$ and $\chi$, and division of $\mathbf{V}_g$

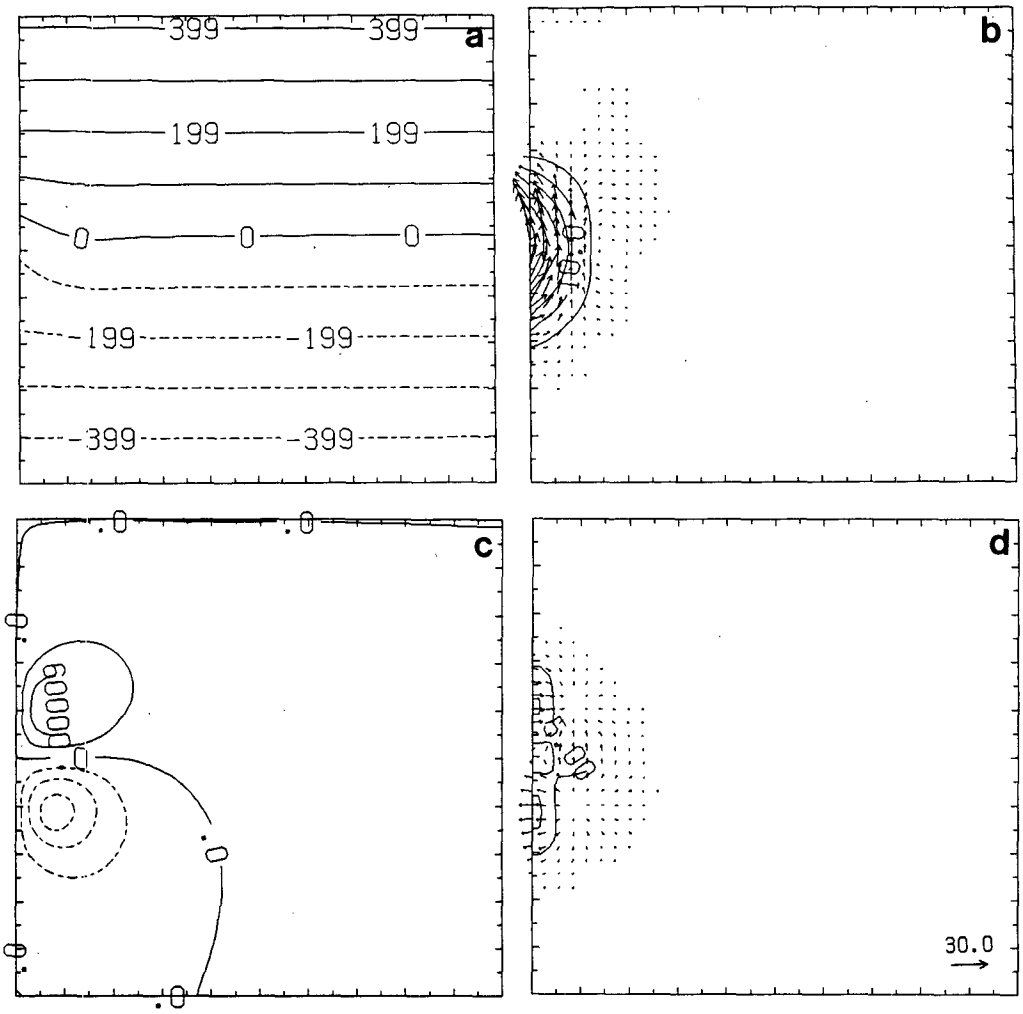


FIG. 8. Results from Experiment 5: (a) Streamfunction field $\psi$ ($10^4$ m$^2$ s$^{-1}$); (b) $\mathbf{V}_\psi - \mathbf{V}_{MSL}$; (c) Potential field $\chi$ (m$^2$ s$^{-1}$); (d) $\mathbf{V}_\chi$. The wind vectors in each figure are scaled by the vector shown in the lower right corner of Fig. 8d, and all vector plots are contoured in isotach intervals of 5 m s$^{-1}$.

into $\mathbf{V}_\psi$ and $\mathbf{V}_\chi$, for the mountain-intersecting-boundary case would be the same as obtained in the right halves of Figs. 4d–4g. The irrotational wind component in Fig. 4g is as strong as $\mathbf{V}_\psi - \mathbf{V}_{MSL}$ (Fig. 4e) over the mountain center. This feature is not reproduced in Experiments 3 and 5 (Figs. 6 and 8). The wind deviations in Experiment 4 (Fig. 7) more closely match the deviations in Experiment 2, although the $\psi$ and $\chi$ fields are then very different between the two experiments. The point of these three experiments is that the $\psi$ and $\chi$ fields, and the resulting division of $\mathbf{V}_g$ into $\mathbf{V}_\psi$ and $\mathbf{V}_\chi$, are very sensitive to their boundary conditions. Any boundary condition implies some arbitrary division of $\mathbf{V}_g$ into $\mathbf{V}_\psi$ and $\mathbf{V}_\chi$. The best way to reduce the effect of this arbitrary division is to place the boundaries where $\mathbf{V}_g$ can be confidently assumed to be mostly nondivergent (or the unlikely opposite, mostly irrotational). Unfortunately, this is not always practical or possible. The Neumann boundary condition (Davies-Jones' natural boundary condition) results in the most generally consistent and reasonable division of $\mathbf{V}_g$ into $\mathbf{V}_\psi$ and $\mathbf{V}_\chi$ on the boundaries.

Finally, the mountain–boundary intersection in the above three experiments is parallel to the thermal wind. Davies-Jones (personal communication, 1988) has pointed out that this orientation is the worst case in terms of compatibility between the solution with the natural boundary condition and the "no-boundary" solution. When the mountain–boundary orientation is perpendicular to the thermal wind, the Neumann boundary condition solution should agree with the "no-boundary" case (Experiment 2 and Fig. 4).

### *b. Boundary condition experiment with the PC method*

The final two experiments illustrate the problem with estimating the Dirichlet-type pressure boundary condition in the PC method. This is related to the standard

pressure reduction problem. Results from using good and bad MSL pressure estimates will be presented in Experiments 6 and 7. The mountain is at the side as in Fig. 5a and the other parameters are the same as in Experiment 1, except that for Experiment 7 the atmosphere has a steeper lapse rate ($\partial T/\partial z = -8.°C$ km$^{-1}$ for Experiment 7 as compared to $-6.5°C$ km$^{-1}$ for Experiment 6). The standard lapse rate estimate ($-6.5°C$ km$^{-1}$) is used for the reduction to MSL around the boundaries for both experiments, thus introducing a significant error in Experiment 7. The deviation of $\mathbf{V}_g$ from $\mathbf{V}_{MSL}$ is shown in Figs. 4c and 2c.

The results are shown in Figs. 9 and 10. Ideally, Figs. 9a and 10a should look similar to the "right half" of Fig. 3c, but they are distorted owing to the error in the boundary conditions. The stronger horizontal pressure gradient at the mountain surface is only slightly reflected in the boundary conditions in Experiment 6, and is distorted by the $\partial\theta/\partial y$ gradient. The

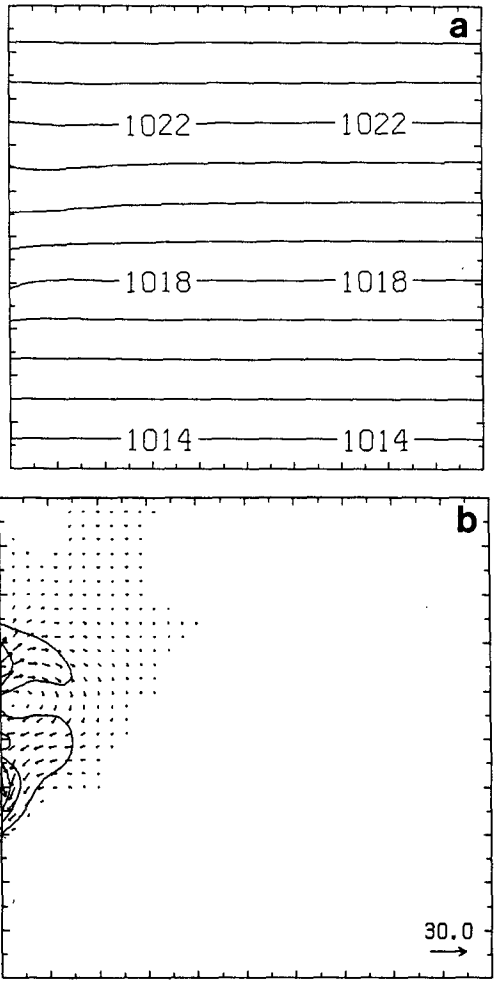


FIG. 9. Results from Experiment 6: (a) PC derived pressure field (mb); (b) $\mathbf{V}_{PC} - \mathbf{V}_{MSL}$. The wind vectors are scaled by the vector shown in the lower right corner of Fig. 9b, and the vector plot is contoured in isotach intervals of 5 m s$^{-1}$.

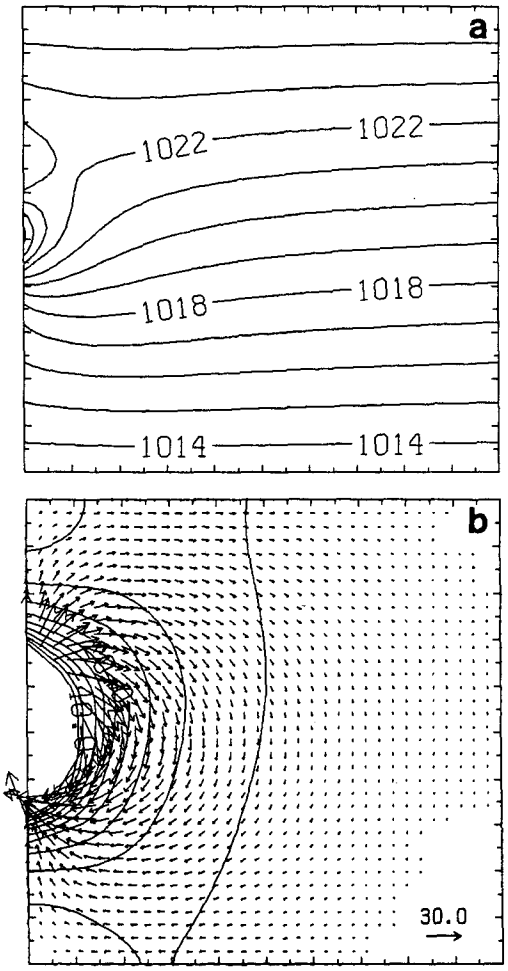


FIG. 10. Results from Experiment 7: (a) PC derived pressure field (mb); (b) $\mathbf{V}_{PC} - \mathbf{V}_{MSL}$. Deviations above 50 m s$^{-1}$ are not plotted (left side of Fig. 10b). The wind vectors are scaled by the vector shown in the lower right corner of Fig. 10b, and the vector plot is contoured in isotach intervals of 5 m s$^{-1}$.

boundary MSL pressure gradient is not as strong or as symmetric as the gradient in Fig. 3c because it has been interpolated downward from a non-uniform (in the $y$ direction) atmosphere. The PC-derived winds ($\mathbf{V}_{PC} - \mathbf{V}_{MSL}$, Fig. 9b) are significantly different from $\mathbf{V}_g - \mathbf{V}_{MSL}$ (Fig. 5c), especially at the boundaries, due to the MSL pressure boundary error.

The results from using the standard atmosphere lapse rate ($\partial T/\partial z = -6.5°C$ km$^{-1}$) in a nonstandard atmosphere ($\partial T/\partial z = -8.°C$ km$^{-1}$) are shown in Fig. 10. The boundary condition error in this case completely obscures the information derived in Experiment 1 and Figs. 3c and 3d. Experiment 7 is an extreme case, and the boundary conditions were chosen to be poor; there are better ways of estimating MSL pressure in areas of elevated terrain (e.g., lapse rates extrapolated downward from above, plateau corrections). The accuracy and utility of the PC method is strongly depen-

dent upon the ability of the boundary conditions (MSL-interpolated pressure) to accurately represent the horizontal pressure gradient at the terrain surface. If a pressure feature (such as a high or low pressure area) or a terrain feature is mostly contained within the interior of the domain of analysis, the PC method will be able to derive the field from its Laplacian information more accurately, and the boundary conditions will be less important. This also applies to the SAN method and Davies-Jones' natural boundary condition.

## 5. Summary

The surface analysis methods of Sangster (1960, 1987) and Pielke and Cram (1987) have been compared numerically. Although the streamfunction (or H) field of Sangster is essentially equivalent to Pielke and Cram's pressure field, the fields are scaled differently and have different sensitivities to their lateral boundary conditions.

The Sangster method consists of decomposing the surface geostrophic wind into streamfunction and potential fields. These fields together give a more complete depiction of the surface geostrophic wind than a single MSL type pressure field, or just the streamfunction. Pielke and Cram's field "looks like" a MSL pressure field and is very similar to a scaled Sangster $\psi$ field, but cannot reflect the information in the irrotational component of the surface geostrophic wind. Pielke and Cram's field depends upon a MSL-reduced pressure for the Dirichlet lateral boundary conditions, and errors in that estimate affect the interior derived field. The lateral boundary conditions for Sangster's streamfunction and potential fields require a division of the surface geostrophic wind at the boundaries into its separate irrotational and nondivergent components. The Neumann boundary conditions for these fields (the natural boundary condition suggested by Davies-Jones 1988) provide more consistent results in general than Dirichlet boundary conditions for these fields. The Dirichlet boundary conditions work well when the boundary curve is level or the boundary winds are nondivergent. A global analysis would eliminate the boundary condition problems for both methods.

*Acknowledgments.* Dr. Dan Keyser is thanked for several very helpful conversations and suggestions in the course of this work. Drs. Robert Davies-Jones and Charles A. Doswell are thanked for their numerous careful reviews of the manuscript, and the early copies of their 1988 papers. Drs. Peter Lynch and Wayne E. Sangster and an anonymous reviewer are also thanked for their comments and suggestions. The authors were supported by NASA Grant NGT-06-002-802 and NSF Grant ATM-8616662. The analyses and graphics were performed on the Colorado State University CYBER 835 and 205 computers.

## REFERENCES

Davies-Jones, R., 1988: On the formulation of surface geostrophic streamfunction. *Mon. Wea. Rev.*, **116,** 1824–1826.

Doswell, C. A. III, 1988: Comments on "An improved technique for computing the horizontal pressure-gradient force at the earth's surface." *Mon. Wea. Rev.*, **116,** 1251–1254.

Lynch, P., 1988: Deducing the wind from vorticity and divergence. *Mon. Wea. Rev.*, **116,** 86–93.

Pielke, R. A., and J. M. Cram, 1987: An alternate procedure for analyzing surface geostrophic winds and pressure over elevated terrain. *Weather and Forecasting,* **2,** 229–236.

Sangster, W. E., 1960: A method of representing the horizontal pressure forces without reduction of station pressures to sea level. *J. Meteor.*, **17,** 166–176.

——, 1987: An improved technique for computing the horizontal pressure-gradient force at the earth's surface. *Mon. Wea. Rev.*, **115,** 1358–1368.

U.S. Dept. of Commerce, 1963: *Manual of Barometry.* U.S. Govt. Printing Office, Washington, DC.